Title

Energetic landscape of polycystin channel gating.

Journal

EMBO reports, 24(7)

ISSN

1469-221X

Authors

Ng, Leo Ct
Harris, Brandon J
Larmore, Megan
et al.

Publication Date

2023-07-01

DOI

10.15252/embr.202356783

Peer reviewed

Article

SOURCE DATA | TRANSPARENT PROCESS | OPEN ACCESS

EMBO reports

Energetic landscape of polycystin channel gating

Leo CT Ng[1], Brandon J Harris[2,3], Megan Larmore[1], My C Ta[1], Thuy N Vien[1], Valerie L Tokars[1], Vladimir Yarov-Yarovoy[2,4] & Paul G DeCaen[1,*]

Abstract

Members of the polycystin family (PKD2 and PKD2L1) of transient receptor potential (TRP) channels conduct Ca^{2+} and depolarizing monovalent cations. Variants in PKD2 cause autosomal dominant polycystic kidney disease (ADPKD) in humans, whereas loss of PKD2L1 expression causes seizure susceptibility in mice. Understanding structural and functional regulation of these channels will provide the basis for interpreting their molecular dysregulation in disease states. However, the complete structures of polycystins are unresolved, as are the conformational changes regulating their conductive states. To provide a holistic understanding of the polycystin gating cycle, we use computational prediction tools to model missing PKD2L1 structural motifs and evaluate more than 150 mutations in an unbiased mutagenic functional screen of the entire pore module. Our results provide an energetic landscape of the polycystin pore, which enumerates gating sensitive sites and interactions required for opening, inactivation, and subsequent desensitization. These findings identify the external pore helices and specific cross-domain interactions as critical structural regulators controlling the polycystin ion channel conductive and nonconductive states.

Keywords calcium; polycystic kidney disease; polycystins; structural biology; TRP channels

Subject Categories Membrane & Trafficking; Molecular Biology of Disease

DOI 10.15252/embr.202356783 | Received 5 January 2023 | Revised 6 April 2023 | Accepted 19 April 2023 | Published online 9 May 2023

EMBO Reports (2023) 24: e56783

Introduction

Polycystins are ion channel subunits whose members can be separated into two groups by homology—those that are related to PKD1 (PKD1, PKD1L1, PKD1L3, and PKDREJ) and those related to PKD2 (PKD2, PKD2L1, and PKD2L2; Nomura *et al*, 1998; Wu *et al*, 1998; Hughes *et al*, 1999; Veldhuisen *et al*, 1999; Guo *et al*, 2000; Li *et al*, 2003; Esarte Palomero *et al*, 2023). PKD1-related subunits have 11 transmembrane segments and do not form channels when expressed alone. However, they may oligomerize with PKD2-related members to form heterotetrameric complexes (e.g., PKD1-PKD2) with combined channel and adhesion G-protein-coupled receptor features (Su *et al*, 2018a, 2021). However, there is only a limited functional understanding of heteromeric polycystins beyond their proposed ligand- or autoproteolytic regulation (Promel *et al*, 2013; Maser *et al*, 2022). In contrast, PKD2-related subunits comprise the polycystin subfamily of transient receptor potential (TRPP) ion channels and form homotetrameric pores that are voltage- and calcium-modulated (Shen *et al*, 2016; Kleene & Kleene, 2017; Liu *et al*, 2017). Human variants in PKD2 cause autosomal dominant polycystic kidney disease (ADPKD)—a common, lethal, and monogenetic disorder characterized by profuse kidney cysts that precipitate renal failure (Willey *et al*, 2019). In contrast, murine genetic studies implicate PKD2L1's role in the central nervous system, where the channel influences the excitability of neurons in the hippocampus and spinal cord (Basora *et al*, 2002; Orts-Del'Immagine *et al*, 2016; Yao *et al*, 2016). Constitutive loss of PKD2L1 expression in mice results in phenotypic seizure susceptibility (Yao *et al*, 2016). Thus, understanding the biophysical and molecular mechanisms controlling polycystin channel function is of considerable significance to the etiology of ADPKD and the regulation of neuronal excitability.

In this study, we are interested in determining how homomeric polycystins open their ion-conducting pathway—the so-called "gating" process—to understand the molecular mechanics governing this conformation change in the channel pore. While PKD2 channels function in primary cilia, patch clamping the cilia membranes is a low-throughput method, which prohibits its use in a large-scale mutagenic screen (Kleene & Kleene, 2017; Liu *et al*, 2017). The pore of PKD2L1 is homologous with PKD2 (Fig EV1A) and was selected for our study because it is the only polycystin that forms activatable channels on the plasma membrane when heterologously expressed (DeCaen *et al*, 2013). High-resolution cryo-EM structures of homotetrameric polycystin channels, PKD2 and PKD2L1, have provided a structural foundation for our study (Shen *et al*, 2016; Grieben *et al*, 2017; Wilkes *et al*, 2017; Hulse *et al*, 2018; Su *et al*, 2018b). From this work, conserved features of polycystin biological assembly have emerged. Each of the four subunits contains six transmembrane helices or segments (S1–S6). The first four segments (S1–S4) form a bundle called the voltage sensor domain (VSD). Sitting on the extracellular side of the VSD and threading from S1, the "tetragonal opening for polycystins" (TOP) domain emanates and forms homotypic

1 Department of Pharmacology, Feinberg School of Medicine, Northwestern University, Chicago, IL, USA
2 Department of Physiology and Membrane Biology, University of California, Davis, Davis, CA, USA
3 Biophysics Graduate Group, University of California, Davis, Davis, CA, USA
4 Department of Anesthesiology and Pain Medicine, University of California, Davis, Davis, CA, USA
*Corresponding author. Tel: 312-503-5930; E-mail: paul.decaen@northwestern.edu

intersubunit contacts. Each of the VSDs flanks the central pore domain (PD), which creates the ion-conducting pathway formed by the S5 and S6 of each the four subunits. The selectivity filter is buttressed by two short pore helices (PH1, PH2) that point toward the conducting pathway on the PDs extracellular side. The ion-conducting pathway of PKD2L1 is constricted by residues (^{556}FLA^{558}) near the cytoplasmic end of S6, forming the inner gate. Conserved residues within the selectivity filter (^{522}GDF^{524}) are proposed to form a second gate for polycystin channels, but the function of this external gate in TRPV (Vanilloid) channels has been challenged (Shen *et al*, 2016; Samanta *et al*, 2018; Jara-Oseguera *et al*, 2019).

Recent work implicated interdomain molecular regulation between the VSD and PD that is required for polycystin channel gating (Ng *et al*, 2019). In response to membrane depolarization, each PKD2L1 VSD transfers a single gating charge (K452) found in the S4 (Ng *et al*, 2019). This activation step precedes and is required for opening of the ion-conducting pore (Fig EV1B). In this study, we build from this work by assessing the mechanism of the final steps of the gating cycle—channel opening, inactivation, and desensitization—by conducting a complete multi-pass mutagenic screen of the pore domain (S5-PH1-PH2-S6) and its associated VSD linker (S4–S5 linker). It is important to note that site selection within our screen is unbiased by *a priori* knowledge of the polycystin structures discussed. Rather, our motivating assumption is that an impartial approach will provide a holistic understanding of the energetics controlling conformational changes within the pore, such as sites of allosteric regulation, which would not be apparent by structural inspection alone.

Results

Mutagenic screen identifies the pore helices as structural regulators of channel opening

To assess the overall energies involved, we developed an extensive and unbiased functional screen of the entire pore domain and its associated S4-S5 linker—which together we call the "pore module" (Figs 1A and EV1A). We generated 122 channel constructs expressing alanine substitutions at every position within the pore module (residues 458–580). Alanine was selected because its methyl functional group is small, chemically inert, and has the greatest α-helix propensity—which constitutes 91% of the secondary structure found in the pore module. We then expressed these channels in immortalized human kidney cells and conducted whole cell voltage-clamp experiments designed to assess the mutations impact on channel gating (Fig EV1C–E). Although most channels were functional, 45 alanine substitutions did not support tail current above background levels found in the native cell line (Appendix Table S1). We then retested the loss-of-function sites, this time making constructs with serine and valine substitutions, but only gained functionally from seven valine mutant channels. The remaining 38 nonfunctional mutant sites are excluded from further analysis in this manuscript as their impact on gating could not be assessed using our approach (Appendix Table S2). From the functional 84 mutant channels, we acquired and fit voltage-dependent tail currents to a two-state Boltzmann function (Figs EV1C and D, and EV2). We then factored the resulting slope (Z) and half-maximal of activation ($V_{1/2}$) to calculate the energetics of channel opening from each mutant (G°), an approach previously used in voltage-gated K^+ channel studies (Yifrach & MacKinnon, 2002). The difference in G° between WT and mutant channels was used to compile a global summary of the change in free energy of gating (ΔG°) at each position within the pore module (Fig 1A). To interpret our functional results in a structural context, we sought to map the location of sensitive residues onto the existing PKD2L1 channel structures solved by cryo-EM (Hulse *et al*, 2018; Su *et al*, 2018b). However, the cytoplasmic portion of the pore-lining S6 (561–580 and onward) and the S4-S5 linker (467–479) are undetermined in these structures (Fig EV3A). To address this, we used AlphaFold to structurally predict these missing components (Varadi *et al*, 2022). We generated five PKD2L1 models that all converged on closed states—having an occluded ion-conducting pathway at the intercellular gate (Fig EV3B). We then selected the top scoring structure as our closed state AlphaFold model (Fig EV3A and C). With this more complete structure in hand, we plotted the severity of ΔG° results as color gradations from white to magenta onto the AlphaFold model (Fig 1B). Nearly all (97%) of the alanine and valine substitutions to the pore residues energetically disfavored channel opening (+ΔG°), rather than favored (-ΔG°). While sensitive sites were found throughout the pore module, substitutions with the highest impact unexpectedly concentrated on the extracellular side. Here, several mutations of hydrophobic residues located in the pore loop and pore helices (PH1, PH2) that interface with neighboring subunits caused the most energetically expensive shifts (Figs 1B and EV2). To compare how mutations that alter ΔG° effect the kinetic state of pore closure (τ_{close}), we fit the decay of their tail currents to a single exponential (Fig EV1D). The change in τ_{close} for each mutant compared with WT ($\Delta\tau_{close}$) was plotted relative to the pore module topology and on the AlphaFold structural model (Figs 1A and B, and 2A; Appendix Table S1). Most mutation sites that cause unfavorable effects on the energetics of opening (+ΔG°) also cause an increase in the rate channel closure relative to the WT channel (-$\Delta\tau_{close}$). These results suggest that most pore module mutations stabilize the closed state, or conversely, destabilize the open state. This correlation also supports the hypothesis that voltage-dependent conformational changes within the VSD are coupled to opening of the pore module. However, several proximally located residues on the intracellular and extracellular sides of the pore had the opposite correlation (+ΔG° and +$\Delta\tau_{close}$), effectively disassociating voltage dependence from the kinetics of channel closure (Fig 2A–C). The first is located between the S4-S5 linker site R472A and C-terminal S6 site E569A—sites that were unresolved in the reported cryo-EM structures (Fig 2C). When mapped onto the PKD2L1 AlphaFold structural model, R472 forms an intra-subunit salt-bridge with E569. Mutating these residues to alanine would exclude this interaction, which may disrupt the mechanical coupling of the VSD to the closing and opening of the inner gate actuated by the S4-S5 linker interaction with the S6. The second set of sites, N531 and R534, mapped to the external side of channel on PH2. The side chains of these residues form hydrogen bonds with backbone carbonyls of the finger 2 motif (W259-R261), which extend from adjacent channel subunit's TOP domain (Fig 2D). Taken together, our screen and modeling results identify internal and external sites in the pore module that engages VSD and TOP domains of the channel, respectively. We hypothesize

that these domains may allosterically regulate the channel via the opening of two gates within the pore, as investigated in the next section.

Opening the inner and outer pore gates is energetically coupled

As discussed, the complete structure of the PKD2L1 pore module is unresolved (Hulse *et al*, 2018; Su *et al*, 2018b). We used Rosetta to model PKD2L1 in an open state and predict the S4-S5 linker and extend the C-terminus of the S6, as described in Methods (Figs 3A and EV3A–D) (Huang *et al*, 2011; Wang *et al*, 2016). When comparing the structural transition from the modeled closed (AlphaFold) to open state (Rosetta), hydrophobic plugging residues F556 of the inner gate move into and out of the ion-conducting pathway, respectively (Movie EV1). Below the hydrophobic plug, homotypic hydrogen bonds formed between the side chain carboxamides of N561, which we hypothesize acts to stabilize the closed state (Figs 3A and B, and EV3E). This bond breaks as the PKD2L1 pore transitions to the open state in the Rosetta model, where the N561 carboxamide interacts with the hydroxyl of T469 extending from the S5 of the adjacent monomer (Movie EV2). Alanine, leucine, and serine substitutions to T469 were all nonfunctional in our screen, suggesting that interactions at this site are essential for channel function (Appendix Table S2). The PKD2L1 inner gate radius expands by 1.4 Å, which creates sufficient pore diameter (4.2 Å, total) to support the passage of a fully dehydrated (2.3–2.7 Å) and possibly partially hydrated Na^+, K^+, and Ca^{2+} ions (Figs 3B and EV3B; Rahm *et al*, 2016). The outer gate of the pore is formed by backbone carbonyls of G522, F524, and the side chains of D523. Here, the backbone carbonyl oxygen of F524 and the side chain carboxylate of D523 hydrogen bond across the channel subunits—an interaction that is *not* state-dependent in our modeled structures (Figs 3C and EV3F). The outer gate pore radius dilates 0.9 Å from the closed and open-state modeled structures, which suggests a relatively small conformational change at this gate during pore opening (Fig 3C). To evaluate if the proposed interactions participate in gating, we introduced seven substitutions at outer (D523) and inner gate (N561) residues, which altered their side chain polarity and measured their effect on PKD2L1 function (Appendix Table S1). We observed that mutations at the outer gate followed the expectations postulated by "hydrophobic gate theory" (Aryal *et al*, 2015). Here, mutations preserving hydropathy and hydrogen bond capability normally found at the outer gate (red circles) had the least impact on $\Delta G°$, whereas hydrophobic substitutions (blue circles) caused the greatest energetic expense (Fig 3C). Conversely, we observed the opposite trend from N561 mutations near the inner gate. Amino acid substitutions, which exclude hydrogen bond formation and enhance hydropathy, decreased the energy required to open PKD2L1 (Fig 3B). This observation is consistent with the proposed structural role of the closed-state N561 hydrogen bonding, where removal of this interaction with hydrophobic mutations is expected to be destabilizing and favor channel opening.

Next, we wondered if mutations at the inner and outer gates would affect gating independently or in a coupled fashion—as this distinction helps us to understand if the two gates are working together (Yifrach & MacKinnon, 2002). Since the two sites are separated by > 22 Å, mutations at both locations would expectedly have energetically additive effects (uncoupled) where coupling energy ($\Delta\Delta G°$) would be nearly zero if the gates are functioning independently (Horovitz, 1996). Alternatively, the impact of the two mutations may have non-additive (i.e., coupled) effects on $\Delta\Delta G°$, which would indicate cooperative regulation of channel opening by the inner and outer gates. Our mutant cycle analysis results identified functional coupling between D523A and N561A, as indicated by their significant non-additive coupling energy ($\Delta\Delta G° = +1.28 \pm 0.2$ kcal/mol, Fig 3D and E; Appendix Table S3). To evaluate the fidelity of this method, we selected two sites located within the S4-S5 linker (D476 and G479) to use as controls and conducted cycle analysis with residues of the inner and outer gates. Here, we observed little difference in coupling energy ($\Delta\Delta G° \approx 0$ kcal/mol) from G473A-D523A and G473A-N561A pairs, validating the sensitivity of our approach (Fig 3D and E). In summary, although the modeling data indicate that the inner gate undergoes the greatest conformational change, our functional results demonstrate that the two gates are energetically coupled despite being separated over long distances. These results suggest that opening the pore involves apparent allosteric regulation between the outer and inner gates and/or concerted roles during pore opening.

Inactivation and desensitization are dependent on an interaction between PH1 and S6

Unlike any other member of the TRP family, PKD2L1 undergoes reversible and voltage-dependent inactivation (Figs 4A and EV1B; Shimizu *et al*, 2009, 2017; Numata *et al*, 2017). The voltage of half-maximal inactivation (Inact. $V_{1/2}$) of the WT human PKD2L1 channel is equal to 20.8 ± 2.2 mV (Appendix Table S1; Fig EV2). Studies carried out with various voltage-gated channels have implicated the pore loops and helices as structural regulators of "slow" or "C-type" inactivation—a non-conducting state caused by the collapse of the selectivity filter (Fan *et al*, 1999; Pavlov *et al*, 2005; Abderemane-Ali *et al*, 2019; Reddi *et al*, 2022). Since comparatively little is known regarding the molecular regulation of polycystin channel inactivation, we used our library to screen the pore module for mutation sites that alter this channel state. We observed that sites throughout the pore module cause considerable positive and negative shifts in Inact $\Delta V_{1/2}$ (Fig 4B; Appendix Table S1). Thus, unlike sites that alter $\Delta G°$, inactivation sensitive sites do not aggregate and are diffused within the pore module (Fig EV4). However, two mutations from this screen, F514A located in PH1 and P538A of the S6, completely abolished inactivation (Fig 4A and C, and EV2A and B). When examining our AlphaFold PKD2L1 model, we observed that F514 and P538 side chains interface (distance Cα-Cα = 3.4 Å) each other between subunits (Fig 4D). We hypothesize that alanine mutations at these sites may either disrupt a CH-π bond or intersubunit hydrophobic packing of the pore turret, and that this interaction is essential for channel entry into the inactivated state. To test this, we generated the cysteine double-mutant channel F514C:P538C, which like the single mutants did not inactivate (Fig 4A and C). However, when the cells expressing the double mutant were treated with the bifunctional cysteine cross-linking agent 1,1 methanediyl bismethanethiosulfonate (M1M), voltage-dependent inactivation was reinstated (Fig 4C). The distance between the cysteine sulfhydryl's of F514C and P538C is 3.0 Å when modeled into the AlphaFold PKD2L1 structure, which is within the known modification range of M1M (< 5 Å; Fig 4D) (Green *et al*, 2001). As a control, we evaluated

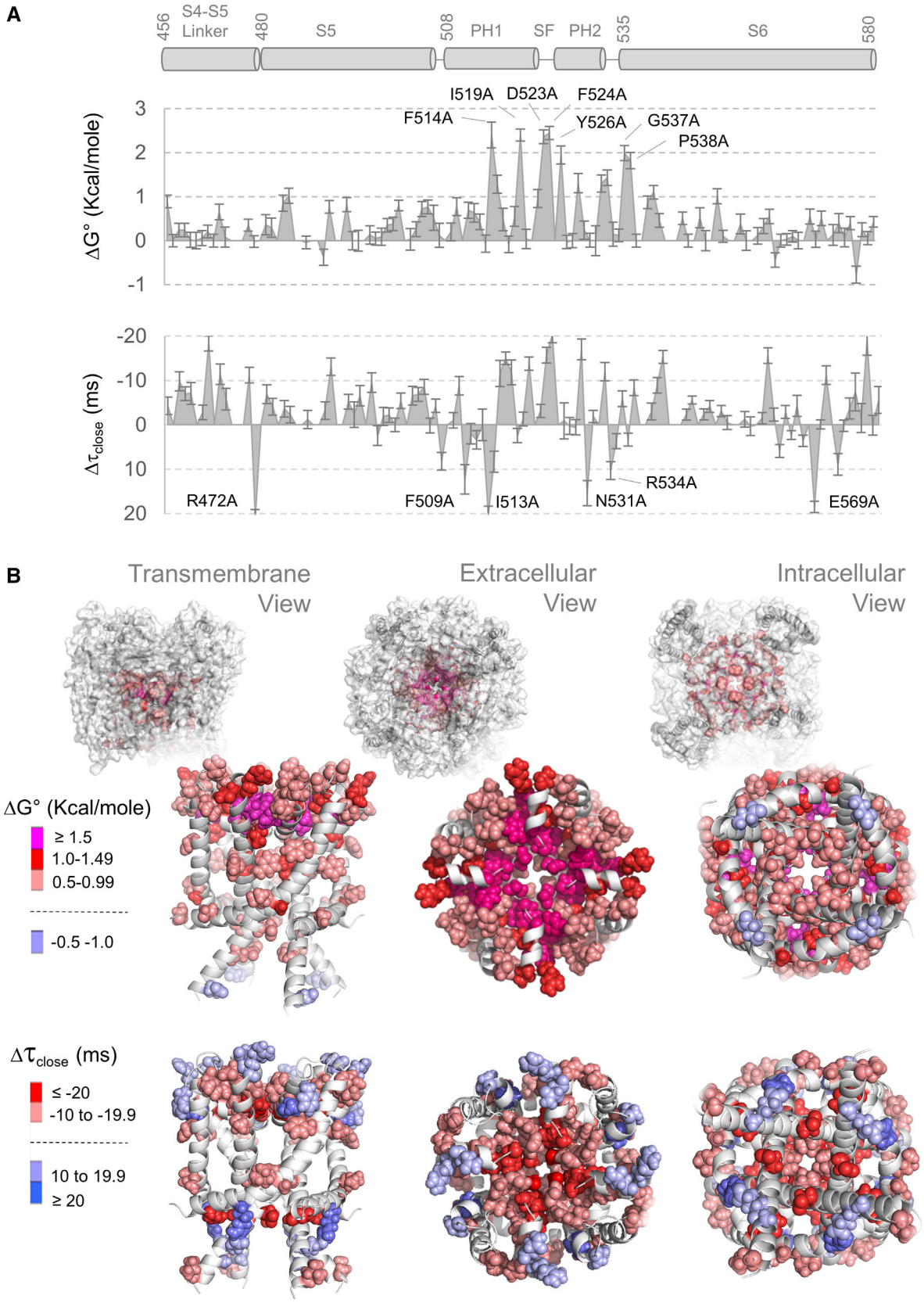

Figure 1.

Figure 1. Functional screen of the PKD2L1 pore module implicates the pore helices in channel gating.

A Perturbation in the free energy of PKD2L1 opening (ΔG°) and difference in closure rates ($\Delta\tau_{close}$) inducted by substitutions within the pore module. ΔG° is estimated from the results shown in Fig EV2 and tabulated in Appendix Table S1. Error bars = SD as estimated by the propagation of error equation, as described in statistics subsection. Mutation sites that produced nonfunctional channels are listed in Appendix Table S2. The number of cells voltage clamped (*N*) for each mutation is indicated within the parenthesis of Fig EV2.

B Heat maps of ΔG° (*top*) and $\Delta\tau_{close}$ (*bottom*) applied on the AlphaFold PKD2L1 channel model. Expanded views of the pore module are shown in the inset, and complete channel structure is shown in the outset. Side chains of high-impact sites are represented as spheres of graduated color intensity, and those from low impact sites are omitted.

Source data are available online for this figure.

voltage-dependent inactivation of WT channels with and without M1M but found no difference in the data generated from both conditions (Fig 4C). Thus, we propose that the observed recovery of inactivation by M1M treatment of the F514C:P538C channels is due to the reinstatement of PH1-S6 intersubunit interactions, which is essential for PKD2L1 inactivation.

PKD2L1 inactivation and calcium-dependent desensitization are distinct functional kinetics (Fig EV1B; DeCaen *et al*, 2016; Shimizu *et al*, 2017). Inactivation is reversible and occurs over the timescale of a few hundred milliseconds, whereas calcium-dependent desensitization is irreversible and develops over 4–7 min as a function of calcium accumulation inside of the cell (Fig 5A and B). Previous work has determined that PKD2L1 desensitization is linked to Ca^{2+} occupancy of the pore selectivity filter (DeCaen *et al*, 2016). Importantly, we observed that all functional mutant channels tested in our pore module screen desensitize within 5 min when 0.81 μM free Ca^{2+} is added into the cytosolic/pipette recording conditions, with the exceptions of F514A and P538A (Fig 5B–D). However, like its effects on voltage-dependent inactivation, M1M reinstated calcium-dependent desensitization of the F514C:P538C double-mutant channel. When comparing the loss of inactivation and desensitization observed in the F514A and P538A channels, the results suggest that desensitization entry is dependent on the channels ability to inactivate. By extension, this finding suggests that desensitization is an irreversible form of inactivation, and that the two non-conducting channel states are structurally related (See Discussion).

Discussion

Structural regulation of polycystin channel opening and the two gate hypothesis

As briefly covered in the introduction, the ion-conducting pathway from the structures of polycystins and several related TRP channels are constricted at inner and outer sites, which are proposed to serve as gates. The single gate hypothesis states that TRP channel pore domains contain one inner gate formed by the crossing of S6 helices, which cooperatively bend to create an iris-like opening along the ion-conducting pathway. The existence of the inner gate is well supported by functional studies of TRP members, including polycystins (Samanta *et al*, 2018). Previous results from voltage clamp studies of heterologously expressed channels in oocytes identified hydrophobic residues, which comprise the inner gate of PKD2L1 (F556, L557, A558; Zheng *et al*, 2018). Our Rosetta and AlphaFold models and results from our voltage clamp studies are consistent with this view, but our work also identifies a symmetric interdomain hydrogen bond ring formed by N561 in the closed state. Neutralization of the side chains proposed to participate in the hydrogen bond results in channels that open with less energy (ΔG°), supporting the hypothesis of this closed-state-dependent interaction at the inner gate. In contrast, the two-gate hypothesis proposes that a second outer gate is also present (G522, D523, F524). While it is accepted that the selectivity filter of TRP channels may undergo dilation in response to continuous ligand stimulation, its function as a gate is controversial (Huffer *et al*, 2020). Our results demonstrate that the inner and outer gates are energetically coupled, but our work does not define how allostery coordinates the opening of the inner and putative outer gates. Thus, our conservative interpretation is impartial to either "one-gate" or "two-gate" models. Rather, our results are conceptually peripheral to this debate by demonstrating long-range coupling energetics between these restricted sites within the pore.

Opening of the pore is regulated by internal and external domain interactions

Previous mutagenesis studies have assessed the impact of a few selected sites within the polycystin pore, but our study represents the most comprehensive functional analysis of this structural module published to date (DeCaen *et al*, 2016; Shimizu *et al*, 2017; Zheng *et al*, 2018). Results from our unbiased functional screen identified the extracellular pore helices and loops as gating-sensitive structural motifs within PKD2L1. As identified in the reports of the PKD2L1 cryo-EM structures, the external side of the pore has a restricted negative charge density locally surrounding the hydrated ion conducting pathway (Hulse *et al*, 2018). As proposed, this feature undoubtably attracts incoming cations to the local environment of the pore. However, changes in hydropathy and electrostatics induced by alanine and valine substitutions of pore module residues cannot explain the functional results from our screen. Here, mutations that cause the greatest energetic expense (+ΔG°) localize to the hydrophobic interface between the pore helices of the PKD2L1 subunits. Most of these sites also enhanced the rate of channel closure, functional results which are consistent with destabilizing effects on the open state, or conversely, stabilizing the closed state. On the other side of the pore module, mutations that altered a salt-bridge interactions with the S6 and S4-S5 linker disassociate voltage-dependent opening from the closure rate of the pore. These findings implicate a mechanical coupling between the state of the pore and VSDs on the internal side of the channel. Other decoupling mutations were observed on the external side of the pore at sites where PH2 side chains

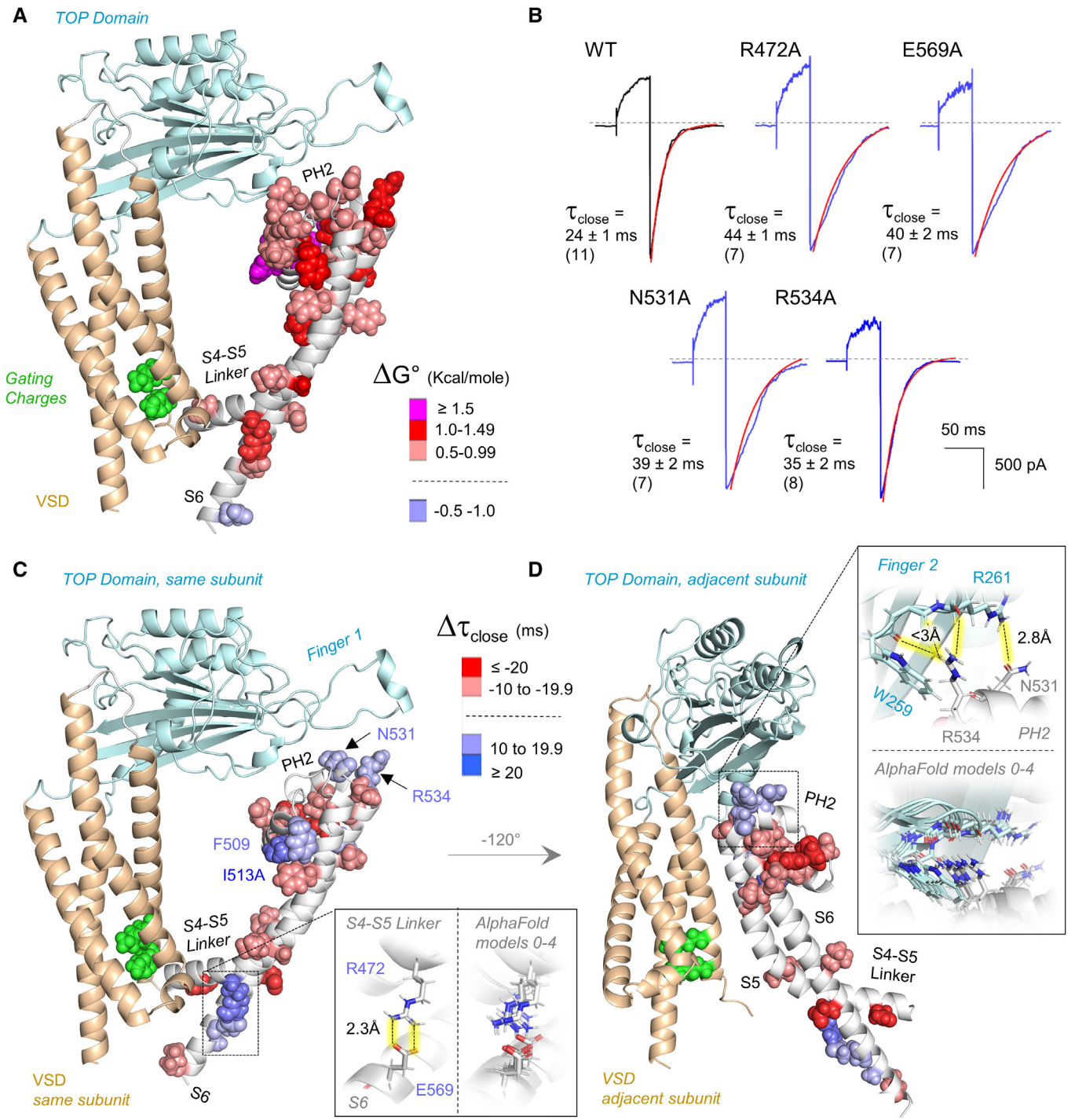

Figure 2. Disrupting internal and external pore module hydrogen bonds disassociate the energetics of opening from the kinetics of channel closure.

A Heat maps of ΔG° applied on to a single PKD2L1 subunit model by AlphaFold.

B Exemplar tail currents from mutant channels where the energetics of opening are disassociated with the rate of channel closure—mutations that cause slower closure ($+\Delta\tau_{close}$) while also increasing the free energy opening ($+\Delta G°$).

C, D Mutations sites that alter $\Delta\tau_{close}$ mapped onto a single PKD2L1 subunit modeled using AlphaFold. *Insets*, expanded views of the intra-subunit salt-bridge formed between the S6 and S4-S5 linker, and the intersubunit hydrogen bond network formed between finger 2 of the TOP domain and PH2 of the adjacent subunits pore module.

Source data are available online for this figure.

form intersubunit hydrogen bonds with the finger 2 motif of the TOP domain. ADPKD-causing missense variants in the finger motifs positively shift PKD2's voltage dependence, which reinforces the hypothesis that the conductive state of the pore is regulated by intersubunit engagement between the VSD and TOP domains (Vien *et al*, 2020). Taken together, these results suggest a cooperative functional link between voltage-dependent movement of the VSD to pore opening via internal S4-S5 linker and external TOP domain structural motifs. Finally, residues that form the gates and participate in interdomain interaction are conserved in PKD2 and PKD2L1 (yellow boxes, Fig EV1A), which suggests that the gating mechanism is shared by both polycystin channels. Future electrophysiology studies assessing the impact of these sites on PKD2 channels measured from the primary cilia

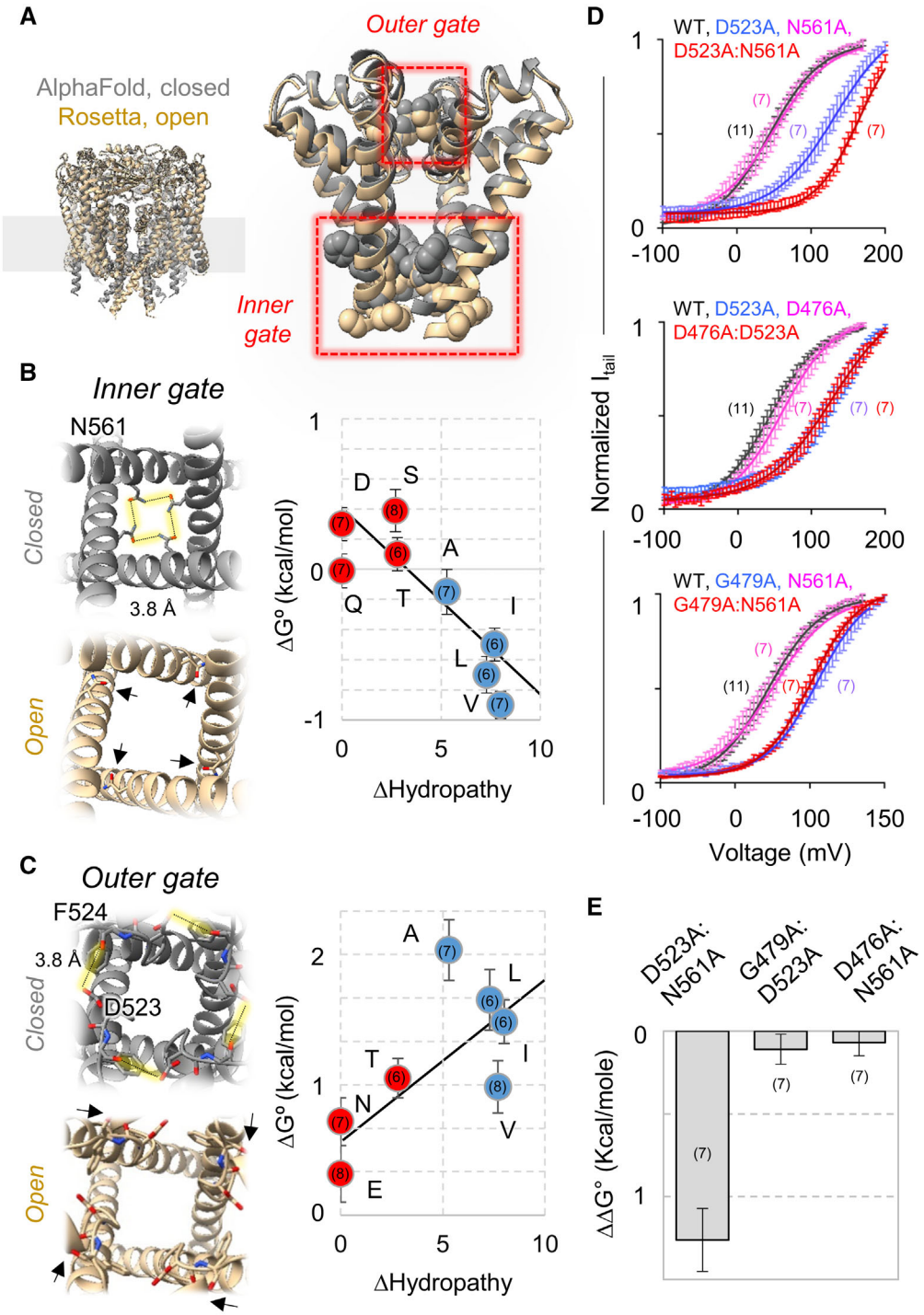

Figure 3.

Figure 3. Inner and outer gates of the pore are energetically coupled.

A AlphaFold and Rosetta modeled PKD2L1 in the open and closed states. Transmembrane view of the channel and an expanded view of the pore domain with the outer and inner gates indicated.

B *Left*, intracellular structural view of the inner gate with an expanded view of the homotypic intersubunit hydrogen bond formed between the carboxamide side chains of N561. *Right*, the linear decreasing relationship between ΔG° and Δhydropathy induced by mutations to D523.

C *Left*, extracellular structural view of the outer gate with an expanded view of the intersubunit hydrogen bond formed between the backbone carbonyl of F524 and the side chain carboxylate of D523. *Right*, linear increasing relationship between ΔG° and change in hydropathy (ΔHydropathy) induced by mutations. Side chains of mutations, which are incapable of forming hydrogen bonds, are indicated in blue.

D Comparing voltage-dependent opening based on normalized tail currents measured from WT, single, and double mutant channels. *Top*, single and double mutant channels including mutations to the outer and inner gate. *Middle* and *bottom*, control groups comparing tail currents from non-gate S4-S5 linker mutations (D476A and G479A) and those from the outer and inner gates.

E The coupling energy (ΔΔG°) resulting from the mutant cycle analysis resulting from the data shown in (D).

Data information: Error bars indicate standard deviation for (B–E) as estimated by the propagation of error equation, as descried in statistics subsection. Number cells tested (*N*) are indicated in parentheses for each group.
Source data are available online for this figure.

membrane will be required to test this hypothesis (DeCaen *et al*, 2013; Liu *et al*, 2017).

Intersubunit interactions with the pore helices are essential for pore inactivation

As discussed, PKD2L1 undergoes voltage-dependent inactivation, a reversible feature shared in Na_v, Ca_v, and K_v channels, but one that sets polycystins apart from other TRP channels (Hoshi *et al*, 1990; Pavlov *et al*, 2005; Abderemane-Ali *et al*, 2019; Reddi *et al*, 2022). Our mutation screen identified numerous sites that shift the voltage dependence of inactivation and ultimately alter channel availability (i.e., closed and not inactivated or desensitized) along the membrane voltage continuum. Inactivation sensitive sites were scattered throughout the pore module of PKD2L1, which indicates that multiple structural motifs influence this channel kinetic. However, we identified only two mutations that completely abolish inactivation and therefore are critical for channel entry into this non-conductive state. F514A in PH1 and P538A in S6 are adjacently located in the modeled and cryo-EM determined structures of PKD2L1 (Hulse *et al*, 2018; Su *et al*, 2018b). Here, we propose that the two residues form a hydrophobic intersubunit interface or CH-π bond based on our bifunctional cysteine cross-linking results at these sites, which reinstated normal inactivation. Previous work identified the N533Q mutation, which also abolished voltage-dependent inactivation and was subsequently localized at the connecting PH2-S6 pore loop in the PKD2L1 cryo-EM structures (Shimizu *et al*, 2017). While the alanine mutation at this same site (N533A) did not abolish inactivation in our hands, it did cause one of the largest shifts ($\Delta V_{1/2}$ inact = 34 mV) in the voltage dependence of inactivation (Appendix Table S1). Based on this previously published work and our results, we propose that interactions made between the S6 and pore helices are critical for entry into the inactivated state. Taken together, these mutations (F514A, N533A, P538A) and possibly other nearby sites can result in significant gain-of-function effects by enhancing channel availability. Such mutations would cause hyperexcitability of hippocampal and spinal cord contacting neurons—tissues that natively express PKD2L1 channels, which regulate high-frequency action potentials (Orts-Del'Immagine *et al*, 2016; Yao *et al*, 2016).

Inactivation and desensitization are distinct non-conducting states that are structurally related

As proposed in our scheme representing PKD2L1 states (Fig EV1B), desensitization is a distinct channel kinetic that is preceded and dependent on channel entry into the inactivated state. Several lines of evidence support this view. First, inactivation is rapid, reversible, and voltage-dependent. Whereas desensitization has a relatively slower kinetic and is dependent on accumulation of internal Ca^{2+}. Structurally, desensitization occurs after a high-affinity interaction with the outer gate/selectivity filter residue D523 (DeCaen *et al*, 2016). Second, we observed that PH1 and S6 mutations, which abolish inactivation (F514A and P538A), also do not desensitize, which demonstrates desensitization dependence on the preceding inactivation step. This supports the possibility that the two

Figure 4. Disrupting an intersubunit CH-π bond between PH1 and S6 abolishes inactivation.

A Gray, voltage protocol used to measure voltage-dependent inactivation. *Black trace*, PKD2L1 currents were activated by a 4 s "prepulse" depolarization in 20 mV increments. A "test pulse" to 120 mV was used to assess the mount of available (non-inactivated) current after the prepulse. *Red trace*, currents activated by the prepulse depolarization to 160 mV. Note, the decrease of the test pulse tail currents (arrow) for the WT and F514C:P538C treated with M2M, whereas the other channel currents remain stable (non-inactivating).

B Summary of the change in voltage-dependent inactivation ($\Delta V_{1/2}$ Inact.) of pore mutant channels. $\Delta V_{1/2}$ Inact., as measured in Fig EV2 and tabulated in Appendix Table S1, are plotted relative to the pore module topology of the channel.

C Voltage-dependent inactivation of test pulse tail currents recorded from WT, single and double mutant channels.

D *Outset*, transmembrane view of the AlphaFold PKD2L1 structural model identifying the non-inactivating mutant sites at the intersubunit interface of the pore turret. *Inset*, expanded views showing Cα-Cα distance between F538 (S6) and F514 (PH1) and modeled sulfur–sulfur distances when cysteine substitutions are made (F514C: P538C).

Data information: All error bars indicate standard deviation and the number cells voltage-clamped (*N*) are indicated in parentheses of Fig EV2.
Source data are available online for this figure.

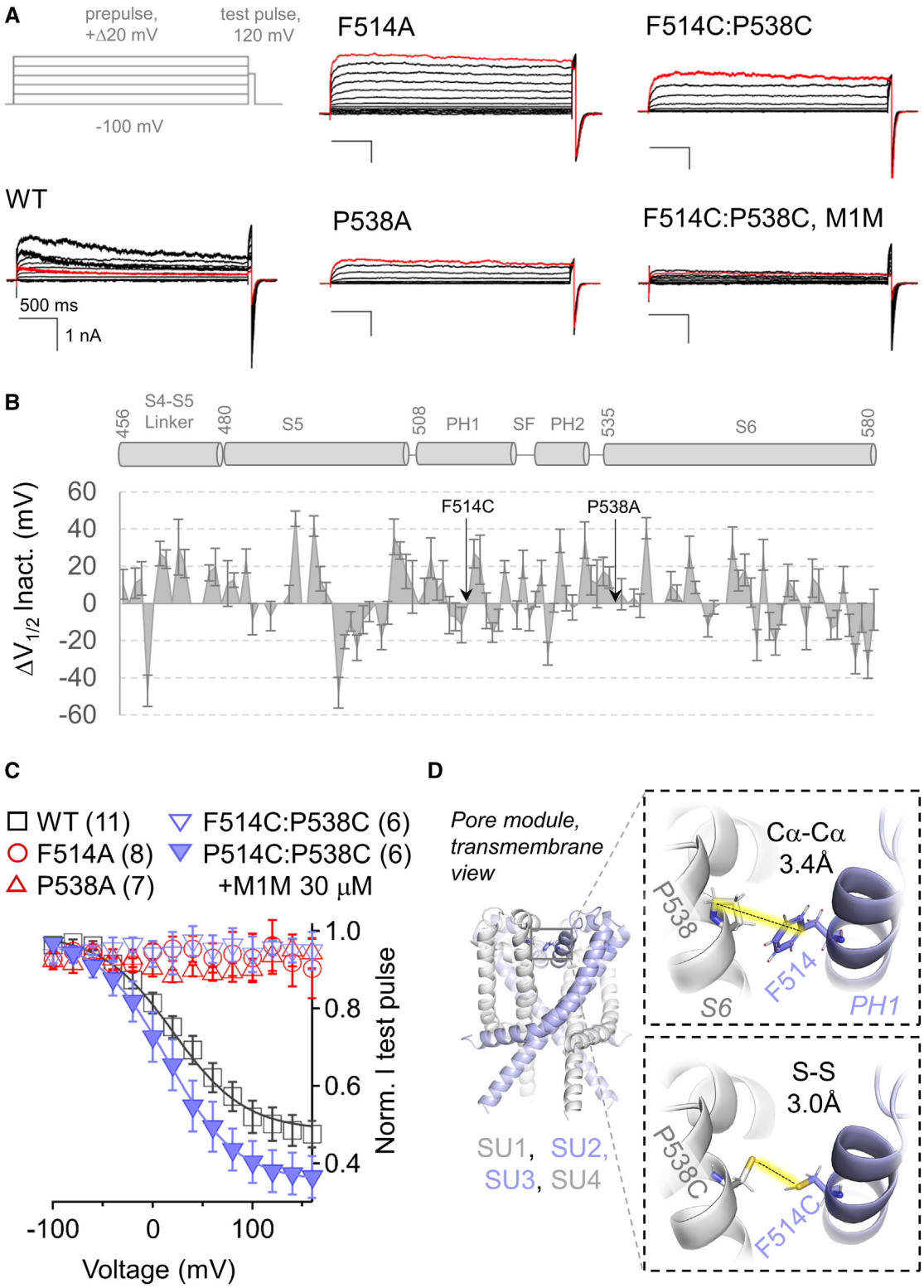

Figure 4.

channel states are structurally related. We speculate that inactivation causes pore collapse at the outer gate and is probably related to C-type inactivation reported in other voltage-gated channels (Fan *et al*, 1999; Pavlov *et al*, 2005; Abderemane-Ali *et al*, 2019; Reddi *et al*, 2022). Since PH1 and PH2 form the structural scaffold of the polycystin outer gate, it seems logical that mutations at these sites could alter desensitization by indirectly disrupting Ca^{2+} binding at this gate. However, future work solving high-resolution structures

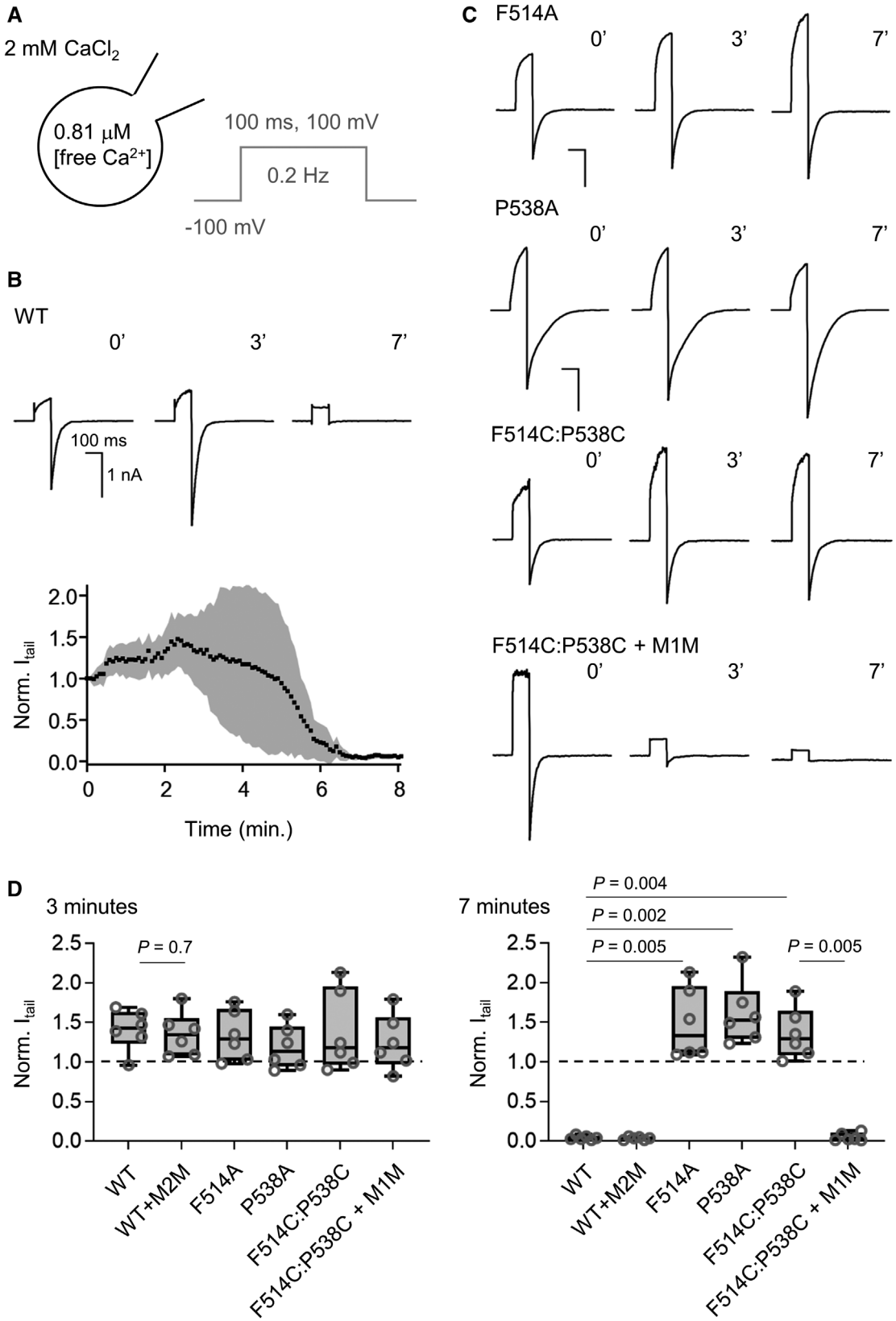

Figure 5.

Figure 5. Abolishing inactivation also eliminates Ca^{2+}-dependent desensitization.

A Schematics of the calcium condition (*Black*) and voltage protocol (*Gray*) that induces Ca^{2+}-dependent desensitization.

B Exemplar WT PKD2L1 current (*Top*) activated by a train of depolarizations to the 0, 3, and 7 min time points. The average time course of PKD2L1 tail current desensitization over 8 min ($N = 6$ cells, gray = SD).

C Exemplar whole cell currents (*Top*) at the 0, 3, and 7 min time points. Current records (*Bottom*) from cells expressing the F514C:P538C and treated with extracellular 100 μM 1,2-methanediyl bismethanethiosulfonate (M2M).

D Box (SEM) and whisker (SD) plots comparing tail currents normalized to their initial amplitude at 3 min (*Left*) and 7-min time points (*Right*). $N = 6$ cells per group. Results from each individual cells are indicated by gray open circles, and the average for the channel is indicated by a horizontal line. *P*-value results from a one-way ANOVA statistical analysis are shown above the plots. Dashed lines the level normalcy, no change in I_{tail} relative to time point zero.

Source data are available online for this figure.

of the polycystins in the inactivated and desensitized states is needed to define the molecular features and chemical interactions responsible for the two non-conducting channel conformations.

Materials and Methods

Voltage-clamp experiments recording plasma membrane PKD2L1 currents

All research chemicals used for our electrophysiology experiments were purchased and supplied Millipore-Sigma, except for 1,1-methanediyl bismethanethiosulfonate, which was supplied by Toronto Research Chemicals. HEK 293T cells (CRL-3216), authenticated by the supplier (ATCC), were transiently transfected (Lipofectamine 2000, Invitrogen) with the mammalian cell expression plasmids pTracer IRES GFP in CMV2 containing the human PKD2L1 gene (isoform 1) or pcdna3.1 with N-terminal HA-tagged PKD2L1 (HA-PKD2L1, isoform 1). Cultured cells were periodically tested for mycoplasma contamination using the PCR reagents provided by ATCC (30-1012K). Transfected cells were seeded onto glass coverslips and placed in a perfusion chamber for voltage clamp recordings in the whole cell configuration. Electrophysiologists were not blinded to the genetic identity of the channel tested. Data were excluded from final analysis if voltage error exceeded 10 mV at the beginning or termination of the experiment. The pipette electrode solution contained (in mM): NaMES (80), NaCl (20), HEPES (10), Na_4-BAPTA (10), and EGTA (5). In desensitization experiments, 0.81 mM free Ca^{2+} was calculated using Maxchelator using 1 M $CaCl_2$ dilution (Bers *et al*, 2010). The standard bath solution contained NaCl (150), HEPES (10), and $CaCl_2$ (2). All our solutions were formulated with ultrapure water (Milli-Q IQ 7005 water), which has $<$ 0.29 ng/l Ca^{2+} ions present. All solutions were pH adjusted to 7.4 with NaOH. The osmolarity of all solutions was measured using an evaporation osmometer (Westcore, Vapro). If needed, internal and external solutions were adjusted to 300 mOs ($\pm$ 5) with mannitol. Whole cell electrodes used to measure PKD2L1 currents were fire polished to 1.5–4 MΩ resistances. Normalized PKD2L1 tail current–voltage relationships were fit to a Boltzmann function to estimate voltage of half-maximal activation of current ($V_{1/2}$), using the following equation: $f(x) = 1/[1 + \exp(V1/2 - Vm)/K]$, where K is equal to the Boltzmann constant. To determine the time course of channel closure ($\tau_{close.}$), tail currents triggered by repolarization were fit using the following exponential equation: $f(x) = B + A \exp[(1/\tau)x]$, where τ is the half time constant. The amount of free energy ($\Delta G°$) required to open WT and mutant channels was calculated using this equation: $\Delta G° = z{\cdot}F{\cdot}V½$, applying voltage-dependent parameters of the Boltzmann equation. Here, F is Faraday's number, z is the estimated charge-based slope derived from K, and $V_{1/2}$ is the half-activation voltage. For our double-mutant cycle analysis, we are assuming that the mutations evaluated only effect the final opening of the channel pore since all the mutations assessed are located within the pore domain. The interaction energy takes into the account the free energy of activation of the wild type (Wt), the individual single mutations (M1, M2), and the double mutant (M1:M2) using the mutant cycle analysis equation:

$$\Delta\Delta G° = (\Delta G_{Wt} + \Delta G_{M1:M2}) - (\Delta G_{M1} + \Delta G_{M2}).$$

Modeling channel structures in closed and open states using AlphaFold and Rosetta

PKD2L1 tetrameric structures (amino acids 90–580) were predicted using AlphaFold V2 multimer structural prediction modeling (doi: https://doi.org/10.1101/2021.10.04.463034) (Varadi *et al*, 2022). Five structural models were determined by AlphaFold, all of which converged on the closed state. We selected the highest ranked structure (model 1) as our "closed state" PKD2L1 model, as its pore domain most closely resembled the diameter of the published closed state cryo-EM structure (Su *et al*, 2018b). For the open-state models, we used Rosetta structural modeling software and the open-state cryo-EM structure (PDB 5Z1W) as a template to model unresolved portions of the PKD2L1 structure (Hulse *et al*, 2018). Loop regions formed by residues 140–148, 174–187, 370–385, and 402–415 in the PKD2L1 closed-state model and residues 372–385 and 457–480 in the PKD2L1 open-state model were modeled *de novo* due to gaps and insertions between sequences of PKD2L1 structures. In total, 10,000 structural models of PKD2L1 channel were generated for each state, and the top 1,000 lowest-scoring models were clustered as described previously (Huang *et al*, 2011; Wang *et al*, 2016). PKD2L1 channel models representing top clusters in each state were chosen as the best models.

PKD2L1 models in an open state were generated using Rosetta Remodel to model the C-terminus. In total, 10,000 cryo-EM refined open-state models were generated, and a representative model was chosen among the top 50 lowest-scoring models with all-atom root mean square deviation (RMSD) $<$ 1.0 Å to open-state PKD2L1 structure (PDB: 5Z1W) and having the lowest side chain RMSD to open-state PKD2L1 structure for inner gate PKD2L1 residues (F556, L557, A558) (Huang *et al*, 2011; Wang *et al*, 2016; Su *et al*, 2018b). The representative open-state model has all-atom RMSD of 0.7 Å to PDB 5Z1W and 0.66 Å side chain RMSD to inner gate residues. Comparative analysis

modeled and cryo-EM determined of the channel pore diameters were calculated using the HOLE program (Smart *et al*, 1996).

Statistics

Unless stated otherwise, all error bars are equal to standard deviation. Propagation of uncertainty (or propagation of error) for ΔG and $\Delta\tau_{1/2}$ was calculated using the following $= \sqrt{(\partial^2 + \partial^2 \ldots)}$, where ∂ is equal to the standard deviation of each measurement. All results were normally distributed per Shapiro–Wilk Test with a P value threshold of 0.1 to reject normalcy. ANOVAs corrected for multiple comparisons with Dunette, and unpaired Students t-tests were calculated using Prism (GraphPad Software, La Jolla, CA). T-test results from data sets with a P value > 0.05 were deemed not significant (N.S.).

Data availability

All unique reagents generated in this study are available by request to the corresponding author. Data reported in this paper are deposited and available at the NU library ARCH (https://doi.org/10.21985/n2-rkpd-p847). Additional information required to reanalyze the data reported in this paper is available from the authors upon request.

Expanded View for this article is available online.

Acknowledgments
We thank Alfonso Mondragon, members of the DeCaen and Yarov-Yarovoy labs for their useful comments during the progress of this study. This work was supported by the National Institute of Diabetes and Digestive and Kidney Diseases (R56DK119709-01, R01DK123463-01, R01 DK131118-01) and the PKD Foundation (Research Grant) awarded to P.G.D. M.L. was supported by NU's Molecular Biophysics Training Program through NIH NIGMS (5T32 GM008382) and National Institute of Diabetes and Digestive and Kidney Diseases of the National Institutes of Health (TL1DK132769). This work used computational resources of the Northwestern University Structural Biology Facility, which is generously supported by NCI CCSG P30 CA060553 grant awarded to the Robert H. Lurie Comprehensive Cancer Center.

Author contributions
Leo CT Ng: Conceptualization; data curation; formal analysis; investigation; writing – original draft; writing – review and editing. **Brandon J Harris:** Formal analysis; validation; investigation; methodology. **Megan Larmore:** Data curation; formal analysis; investigation. **My C Ta:** Data curation; formal analysis. **Thuy N Vien:** Formal analysis; investigation. **Valerie L Tokars:** Data curation; formal analysis. **Vladimir Yarov-Yarovoy:** Conceptualization; formal analysis; investigation; methodology. **Paul G DeCaen:** Conceptualization; validation; writing – original draft; project administration; writing – review and editing.

Disclosure and competing interests statement
The authors declare that they have no conflict of interest.

References

Abderemane-Ali F, Findeisen F, Rossen ND, Minor DL Jr (2019) A selectivity filter gate controls voltage-gated Calcium Channel calcium-dependent inactivation. *Neuron* 101: 1134–1149.e3

Aryal P, Sansom MS, Tucker SJ (2015) Hydrophobic gating in ion channels. *J Mol Biol* 427: 121–130

Basora N, Nomura H, Berger UV, Stayner C, Guo L, Shen X, Zhou J (2002) Tissue and cellular localization of a novel polycystic kidney disease-like gene product, polycystin-L. *J Am Soc Nephrol* 13: 293–301

Bers DM, Patton CW, Nuccitelli R (2010) A practical guide to the preparation of Ca(2+) buffers. *Methods Cell Biol* 99: 1–26

DeCaen PG, Delling M, Vien TN, Clapham DE (2013) Direct recording and molecular identification of the calcium channel of primary cilia. *Nature* 504: 315–318

DeCaen PG, Liu X, Abiria S, Clapham DE (2016) Atypical calcium regulation of the PKD2-L1 polycystin ion channel. *Elife* 5: e13413

Esarte Palomero O, Larmore M, DeCaen PG (2023) Polycystin Channel complexes. *Annu Rev Physiol* 85: 425–448

Fan JS, Jiang M, Dun W, McDonald TV, Tseng GN (1999) Effects of outer mouth mutations on hERG channel function: a comparison with similar mutations in the shaker channel. *Biophys J* 76: 3128–3140

Green NS, Reisler E, Houk KN (2001) Quantitative evaluation of the lengths of homobifunctional protein cross-linking reagents used as molecular rulers. *Protein Sci* 10: 1293–1304

Grieben M, Pike AC, Shintre CA, Venturi E, El-Ajouz S, Tessitore A, Shrestha L, Mukhopadhyay S, Mahajan P, Chalk R *et al* (2017) Structure of the polycystic kidney disease TRP channel Polycystin-2 (PC2). *Nat Struct Mol Biol* 24: 114–122

Guo L, Schreiber TH, Weremowicz S, Morton CC, Lee C, Zhou J (2000) Identification and characterization of a novel polycystin family member, polycystin-L2, in mouse and human: sequence, expression, alternative splicing, and chromosomal localization. *Genomics* 64: 241–251

Horovitz A (1996) Double-mutant cycles: a powerful tool for analyzing protein structure and function. *Fold Des* 1: R121–R126

Hoshi T, Zagotta WN, Aldrich RW (1990) Biophysical and molecular mechanisms of shaker potassium channel inactivation. *Science* 250: 533–538

Huang PS, Ban YE, Richter F, Andre I, Vernon R, Schief WR, Baker D (2011) RosettaRemodel: a generalized framework for flexible backbone protein design. *PLoS One* 6: e24109

Huffer KE, Aleksandrova AA, Jara-Oseguera A, Forrest LR, Swartz KJ (2020) Global alignment and assessment of TRP channel transmembrane domain structures to explore functional mechanisms. *Elife* 9: e58660

Hughes J, Ward CJ, Aspinwall R, Butler R, Harris PC (1999) Identification of a human homologue of the sea urchin receptor for egg jelly: a polycystic kidney disease-like protein. *Hum Mol Genet* 8: 543–549

Hulse RE, Li Z, Huang RK, Zhang J, Clapham DE (2018) Cryo-EM structure of the polycystin 2-l1 ion channel. *Elife* 7: e36931

Jara-Oseguera A, Huffer KE, Swartz KJ (2019) The ion selectivity filter is not an activation gate in TRPV1-3 channels. *Elife* 8: e51212

Kleene SJ, Kleene NK (2017) The native TRPP2-dependent channel of murine renal primary cilia. *Am J Physiol Renal Physiol* 312: F96–F108

Li A, Tian X, Sung SW, Somlo S (2003) Identification of two novel polycystic kidney disease-1-like genes in human and mouse genomes. *Genomics* 81: 596–608

Liu X, Vien T, Duan J, Sheu S-H, DeCaen PG, Clapham DE (2017) Polycystin-2 is an essential ion channel subunit in the primary cilium of the renal collecting duct epithelium. *Elife* 7: e33183

Maser RL, Calvet JP, Parnell SC (2022) The GPCR properties of polycystin-1- a new paradigm. *Front Mol Biosci* 9: 1035507

Ng LCT, Vien TN, Yarov-Yarovoy V, DeCaen PG (2019) Opening TRPP2 (PKD2L1) requires the transfer of gating charges. *Proc Natl Acad Sci USA* 116: 15540–15549

Nomura H, Turco AE, Pei Y, Kalaydjieva L, Schiavello T, Weremowicz S, Ji W, Morton CC, Meisler M, Reeders ST *et al* (1998) Identification of PKDL, a novel polycystic kidney disease 2-like gene whose murine homologue is deleted in mice with kidney and retinal defects. *J Biol Chem* 273: 25967–25973

Numata T, Tsumoto K, Yamada K, Kurokawa T, Hirose S, Nomura H, Kawano M, Kurachi Y, Inoue R, Mori Y (2017) Integrative approach with electrophysiological and theoretical methods reveals a new role of S4 positively charged residues in PKD2L1 channel voltage-sensing. *Sci Rep* 7: 9760

Orts-Del'Immagine A, Seddik R, Tell F, Airault C, Er-Raoui G, Najimi M, Trouslard J, Wanaverbecq N (2016) A single polycystic kidney disease 2-like 1 channel opening acts as a spike generator in cerebrospinal fluid-contacting neurons of adult mouse brainstem. *Neuropharmacology* 101: 549–565

Pavlov E, Bladen C, Winkfein R, Diao C, Dhaliwal P, French RJ (2005) The pore, not cytoplasmic domains, underlies inactivation in a prokaryotic sodium channel. *Biophys J* 89: 232–242

Promel S, Langenhan T, Arac D (2013) Matching structure with function: the GAIN domain of adhesion-GPCR and PKD1-like proteins. *Trends Pharmacol Sci* 34: 470–478

Rahm M, Hoffmann R, Ashcroft NW (2016) Atomic and ionic radii of elements 1-96. *Chemistry* 22: 14625–14632

Reddi R, Matulef K, Riederer EA, Whorton MR, Valiyaveetil FI (2022) Structural basis for C-type inactivation in a shaker family voltage-gated K(+) channel. *Sci Adv* 8: eabm8804

Samanta A, Hughes TET, Moiseenkova-Bell VY (2018) Transient receptor potential (TRP) channels. *Subcell Biochem* 87: 141–165

Shen PS, Yang X, DeCaen PG, Liu X, Bulkley D, Clapham DE, Cao E (2016) The structure of the polycystic kidney disease channel PKD2 in lipid nanodiscs. *Cell* 167: 763–773.e11

Shimizu T, Janssens A, Voets T, Nilius B (2009) Regulation of the murine TRPP3 channel by voltage, pH, and changes in cell volume. *Pflugers Arch* 457: 795–807

Shimizu T, Higuchi T, Toba T, Ohno C, Fujii T, Nilius B, Sakai H (2017) The asparagine 533 residue in the outer pore loop region of the mouse PKD2L1 channel is essential for its voltage-dependent inactivation. *FEBS Open Bio* 7: 1392–1401

Smart OS, Neduvelil JG, Wang X, Wallace BA, Sansom MS (1996) HOLE: a program for the analysis of the pore dimensions of ion channel structural models. *J Mol Graph* 14: 376–360

Su Q, Hu F, Ge X, Lei J, Yu S, Wang T, Zhou Q, Mei C, Shi Y (2018a) Structure of the human PKD1-PKD2 complex. *Science* 361: eaat9819

Su Q, Hu F, Liu Y, Ge X, Mei C, Yu S, Shen A, Zhou Q, Yan C, Lei J *et al* (2018b) Cryo-EM structure of the polycystic kidney disease-like channel PKD2L1. *Nat Commun* 9: 1192

Su Q, Chen M, Wang Y, Li B, Jing D, Zhan X, Yu Y, Shi Y (2021) Structural basis for Ca(2+) activation of the heteromeric PKD1L3/PKD2L1 channel. *Nat Commun* 12: 4871

Varadi M, Anyango S, Deshpande M, Nair S, Natassia C, Yordanova G, Yuan D, Stroe O, Wood G, Laydon A *et al* (2022) AlphaFold protein structure database: massively expanding the structural coverage of protein-sequence space with high-accuracy models. *Nucleic Acids Res* 50: D439–D444

Veldhuisen B, Spruit L, Dauwerse HG, Breuning MH, Peters DJ (1999) Genes homologous to the autosomal dominant polycystic kidney disease genes (PKD1 and PKD2). *Eur J Hum Genet* 7: 860–872

Vien TN, Wang J, Ng LCT, Cao E, DeCaen PG (2020) Molecular dysregulation of ciliary polycystin-2 channels caused by variants in the TOP domain. *Proc Natl Acad Sci USA* 117: 10329–10338

Wang RY, Song Y, Barad BA, Cheng Y, Fraser JS, DiMaio F (2016) Automated structure refinement of macromolecular assemblies from cryo-EM maps using Rosetta. *Elife* 5: e17219

Wilkes M, Madej MG, Kreuter L, Rhinow D, Heinz V, De Sanctis S, Ruppel S, Richter RM, Joos F, Grieben M *et al* (2017) Molecular insights into lipid-assisted Ca(2+) regulation of the TRP channel Polycystin-2. *Nat Struct Mol Biol* 24: 123–130

Willey C, Kamat S, Stellhorn R, Blais J (2019) Analysis of Nationwide data to determine the incidence and diagnosed prevalence of autosomal dominant polycystic kidney disease in the USA: 2013–2015. *Kidney Dis (Basel)* 5: 107–117

Wu G, Hayashi T, Park JH, Dixit M, Reynolds DM, Li L, Maeda Y, Cai Y, Coca-Prados M, Somlo S (1998) Identification of PKD2L, a human PKD2-related gene: tissue-specific expression and mapping to chromosome 10q25. *Genomics* 54: 564–568

Yao G, Luo C, Harvey M, Wu M, Schreiber TH, Du Y, Basora N, Su X, Contreras D, Zhou J (2016) Disruption of polycystin-L causes hippocampal and thalamocortical hyperexcitability. *Hum Mol Genet* 25: 448–458

Yifrach O, MacKinnon R (2002) Energetics of pore opening in a voltage-gated K(+) channel. *Cell* 111: 231–239

Zheng W, Yang X, Hu R, Cai R, Hofmann L, Wang Z, Hu Q, Liu X, Bulkley D, Yu Y *et al* (2018) Hydrophobic pore gates regulate ion permeation in polycystic kidney disease 2 and 2L1 channels. *Nat Commun* 9: 2302